Sensors and Actuators A 164 (2010) 58–67

Contents lists available at ScienceDirect

Sensors and Actuators A: Physical

journal homepage: www.elsevier.com/locate/sna

Thermo-mechanical properties of alumina films created using the atomic layer deposition technique

David C. Miller[a,d,*], Ross R. Foster[a,d], Shih-Hui Jen[b,d], Jacob A. Bertrand[b,d], Shawn J. Cunningham[c,d], Arthur S. Morris[c,d], Yung-Cheng Lee[a,d], Steven M. George[b,d], Martin L. Dunn[a,d]

[a] Department of Mechanical Engineering, University of Colorado, Boulder, CO 80309, USA
[b] Department of Chemistry and Biochemistry, University of Colorado, Boulder, CO 80309, USA
[c] WiSpry, Inc., Irvine, CA 92618, USA
[d] DARPA Center for Integrated Micro/Nano-Electromechanical Transducers (iMINT), University of Colorado, Boulder, CO 80309, USA

ARTICLE INFO

Article history:
Received 8 March 2010
Received in revised form
11 September 2010
Accepted 22 September 2010
Available online 29 September 2010

Keywords:
Thin film
Mechanical properties
Reliability
Robustness

ABSTRACT

Interdigitated humidity sensors with atomic layer deposited (ALD) coatings of aluminum oxide demonstrated no leakage current relative to uncoated sensors stored in the ambient, indicating Al_2O_3 may be used to limit the effects of H_2O and other chemical species in miniaturized mechanical- and electronic-devices. The long term durability of such coatings is not known, but may be predicted from the related material characteristics. The modulus and hardness of Al_2O_3 were therefore measured by nanoindentation using a Berkovich tip. Because the coatings are brittle and possess a significant tensile stress, the influence of film stress on the indentation measurements was quantified using a numerical analysis protocol, which also considered the effect of substrate compliance. The film stress and coefficient of thermal expansion for Al_2O_3 were determined using the wafer curvature method. Film stress was characterized using thermal cycling up to 500 °C. Separate $Si/SiO_2/Si$ microcantilever arrays demonstrated a stress variation according to the thickness of Al_2O_3 coatings. Fracture toughness was examined by indentation with a cube-corner tip; the estimates are subject to film stress and the material-dependent geometry factor.

1. Introduction

The atomic layer deposition (ALD) technique [1–4] may be used to grow thin metallic or ceramic films. ALD ceramic coatings have found application as high κ dielectrics within the field of integrated circuit technology [5]. ALD coatings have been proposed to be utilized in a broad range of applications, including the encapsulation of compliant substrates [6–8] as well as the surface functionalization of: nano-particles or nano-tubes [9,10], porous films/membranes [10,11], and microsystems [12,13]. Such coatings may be used to tailor characteristics including: chemical permeation, charge-dissipation, surface-adhesion, corrosion resistance, or tribological behavior [13]. ALD coatings are expected to benefit from the characteristics unique to the deposition technique: the resulting films are continuous, conformal, pin-hole free, and may be grown with sub-nanometer thickness control.

The previously unstudied thermo-mechanical properties are essential to the design and engineering of reliable components containing ALD films. Instrumented indentation [14,15] is a popular technique that has been employed to study a broad variety of thin films. Properties, such as modulus and hardness, may be determined from the measured load vs. depth relationship when a prescribed tip is impressed into a specimen. The mechanical response for a film is, however, only automatically decoupled from its host substrate at indentation depths that are significantly less than that of the film thickness [16]. Owing to the limitations of the technique including: the tip (capability of its manufacture and wear from use), the specimen (surface roughness, surface contamination, and alignment with respect to the tip), and the indent region (the evolution if its initial geometry and the stress distribution), the indenter tip must typically be pressed into the specimen by at least 50 nm before the raw modulus and hardness measurements have stabilized [17]. Practically speaking, these considerations imply the film must be at least 500 nm thick to obtain accurate raw measurements.

In addition to the common Berkovich tip (where a 65.30° physical angle on faces results in an 8% constant strain [15]), a cube-corner tip may be used (where 35.26° physical angle results in an 18% applied strain [18]). The measured E and H values as well as the variability may be affected for the cube-corner tip for rea-

* Corresponding author at: National Center for Photovoltaics, National Renewable Energy Laboratory, 1617 Cole Boulevard, MS-3214, Golden, CO 80401-3214, USA. Tel.: +1 303 384 7855; fax: +1 303 384 6490.
E-mail address: David.Miller@nrel.gov (D.C. Miller).

0924-4247/$ – see front matter © 2010 Elsevier B.V. All rights reserved.
doi:10.1016/j.sna.2010.09.018

Report Documentation Page

Form Approved
OMB No. 0704-0188

1. REPORT DATE	2. REPORT TYPE	3. DATES COVERED
SEP 2010		**00-00-2010 to 00-00-2010**

4. TITLE AND SUBTITLE	5a. CONTRACT NUMBER
Thermo-mechanical properties of alumina films created using the atomic layer deposition technique	5b. GRANT NUMBER
	5c. PROGRAM ELEMENT NUMBER
6. AUTHOR(S)	5d. PROJECT NUMBER
	5e. TASK NUMBER
	5f. WORK UNIT NUMBER
7. PERFORMING ORGANIZATION NAME(S) AND ADDRESS(ES) **University of Colorado,Department of Chemistry and Biochemistry,Boulder,CO,80309**	8. PERFORMING ORGANIZATION REPORT NUMBER
9. SPONSORING/MONITORING AGENCY NAME(S) AND ADDRESS(ES)	10. SPONSOR/MONITOR'S ACRONYM(S)
	11. SPONSOR/MONITOR'S REPORT NUMBER(S)

12. DISTRIBUTION/AVAILABILITY STATEMENT
Approved for public release; distribution unlimited

13. SUPPLEMENTARY NOTES

14. ABSTRACT

Interdigitated humidity sensors with atomic layer deposited (ALD) coatings of aluminum oxide demonstrated no leakage current relative to uncoated sensors stored in the ambient, indicating Al2O3 may be used to limit the effects of H2O and other chemical species in miniaturized mechanical- and electronicdevices. The long term durability of such coatings is not known, but may be predicted from the related material characteristics. The modulus and hardness of Al2O3 were therefore measured by nanoindentation using a Berkovich tip. Because the coatings are brittle and possess a significant tensile stress, the influence of film stress on the indentation measurements was quantified using a numerical analysis protocol which also considered the effect of substrate compliance. The film stress and coefficient of thermal expansion for Al2O3 were determined using the wafer curvature method. Film stress was characterized using thermal cycling up to 500 ◦C. Separate Si/SiO2/Si microcantilever arrays demonstrated a stress variation according to the thickness of Al2O3 coatings. Fracture toughness was examined by indentation with a cube-corner tip; the estimates are subject to film stress and the material-dependent geometry factor.

15. SUBJECT TERMS

16. SECURITY CLASSIFICATION OF:			17. LIMITATION OF ABSTRACT	18. NUMBER OF PAGES	19a. NAME OF RESPONSIBLE PERSON
a. REPORT **unclassified**	b. ABSTRACT **unclassified**	c. THIS PAGE **unclassified**	**Same as Report (SAR)**	**10**	

sons including material anisotropy and greater pile-up at the tip [19]. The greater applied strain for a cube-corner tip enhances the likelihood of radial crack formation.

The technique of fracture toughness estimation via indentation pioneered by Lawn and others [20–22] requires the impression site to be imaged. The technique relies on the assumption that only the depth of the impression recovers during unloading, whereas the length of the impressional diagonals and the radial cracks remain unchanged. The technique originally applied to shallow indentation (crack depths $\leq 0.4h_f$) using a Vickers tip [22,23], but has been extended to the Berkovich [24] and cube-corner [25] tips. Crack depth, which determines the analysis model, equals $(c-a)/2$ as corner cracks (generated during loading or at the start of unloading) typically have a semicircular profile when viewed in cross-section [22,23]. Eq. (1) relates between fracture toughness and the observed morphology for deep indentation (crack depths $\geq 0.7h_f$) [26].

$$K = \left(\lambda \frac{(E_f H_f^2)^{1/3}}{h_f} \frac{a^2}{c^{1/2}}\right) + (g[D_1, D_2]\sigma_f(\pi h_f)^{0.5}) \quad (1)$$

In the equation, here for system international (SI) units, K represents the fracture toughness (MPa $m^{0.5}$); λ the empirical tip geometry factor – here the default value of 0.040 (unitless) [25]; E the modulus from indentation (Pa); H the hardness from indentation (Pa); π the mathematical constant (3.142); h the thickness (m); a the distance from the tip to the corner within the impression (m); c the distance from the impression corner to the end of the crack (m); the coefficient g accounts for elastic misfit between the film and substrate (unitless) [27]; D represents the Dunder's parameters (unitless) [28]; and σ the stress (Pa). The subscript f refers to the film. For deep impressions to qualify for examination, cracks must be of sufficient length, i.e. $(c-a) \geq 4h_f$, which corresponds to the condition of steady state channel-crack propagation [29,30]. A more rigorous model has recently been developed for estimating toughness from channel-cracked films [31], where a solution may be obtained if the true- and apparent-film modulus, maximum load, and other parameters in Eq. (1) are known for 2 or more indentation depths.

The curvature of a film/substrate system is often used to examine σ_f as well as the coefficient of thermal expansion (CTE). Stoney's solution [32,33] relates between curvature and stress in a thin film deposited on a thick substrate, Eq. (2).

$$\sigma_f = \frac{E_s {h_s}^2}{6(1-\upsilon_s)h_f}\Delta\kappa \quad (2)$$

For curvature vs. temperature profiles, CTE can be evaluated using Eq. (3) [33].

$$\Delta\kappa = \frac{6(1-\upsilon_s)h_f E_f(\alpha_s - \alpha_f)\Delta T}{(1-\upsilon_f)E_s {h_s}^2} \quad (3)$$

New parameters in the equations include κ, which represents the curvature (m^{-1}); ν the Poisson's ratio (unitless); α the CTE (ppm/°C); and T the temperature (°C). The subscripts f and s refer to the film and substrate, respectively. In practice, the uncoated substrate is not perfectly flat. Then, Eq. (2) may be evaluated from the difference in R, the radius of curvature (m), present before and after deposition, $\Delta\kappa = (1/R_a) - (1/R_b)$. In the analysis, the film is assumed to be of uniform thickness, and σ_f is equibiaxial and constant throughout h_f. If h_f is not two orders of magnitude less than h_s, or for a stiff film on a compliant substrate, the system may be analyzed as a multilayer composite [34–36]. Such analysis is accurate and may be readily performed without a correction factor [36].

Residual stress is a longstanding concern in the thin film community, and σ_f ranging from 0.5 to 5.5 GPa has been reported for $h_f \leq 500$ nm for Cu, Ni, Ti, Cr, Mo, Ta, TiN, cubic BN, and Ta_2N films [37–43]. σ_f from 3–5.5 GPa was directly verified using X-ray diffraction measurements [40,42]. Stress in physical- and chemical-vapor deposited films frequently demonstrates a complicated profile through the thickness of the film [44–46], owing to the process of island-formation and coalescence [44–48]. Recent study of the ALD process for amorphous materials [49,50] suggests an initial non-linear growth regime, occurring similar to island-formation, followed by steady-state deposition after a contiguous film has formed. The mass accumulated during ALD [51] suggests that either island formation or ubiquitous growth may occur, depending on the propensity for the substrate to promote or hinder film nucleation (i.e., its composition as an oxide or noble metal, respectively).

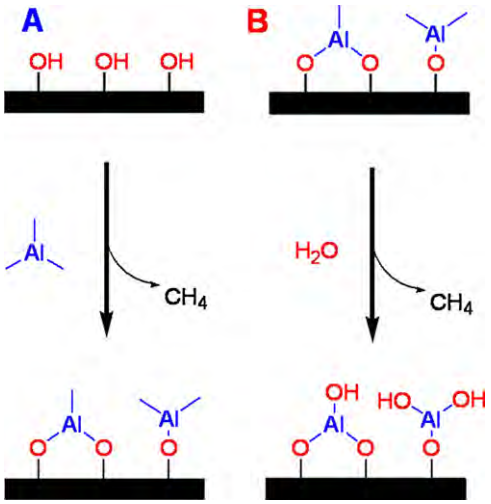

Fig. 1. Schematic showing sub-reaction sequence resulting in the growth of Al_2O_3. Film growth is realized according to the reactant sequence of (a) trimethylaluminum and (b) water.

The examination here was motivated by the use of ALD to create a chemical permeation barrier [8]. Regarding that application, the long term durability of mono- and multi-layer ALD coatings is not known, but may be understood from the related material characteristics. The properties of ALD coatings are not well-established, and may vary significantly from those of bulk material, owing to porosity and other factors [4]. The goal of this study is therefore to examine the thermo-mechanical properties of alumina films, grown using the ALD technique. Specifically, the characteristics of elastic modulus, hardness, film stress, and CTE are examined using indentation and the wafer curvature method. Drawing on the latter technique, film stress is also examined from the curvature of multilayer composite microcantilever beams.

2. Experimental

Films were deposited in a viscous flow reactor using the ALD [1–4] technique. Films are deposited in blanket format, as the technique does not require line-of-sight for deposition. The deposition technique is based on a sequence of two or more self-limiting reactions between vapor-phase precursors and a solid surface. A simple recipe for Al_2O_3 film growth incorporates the two half-reactions, (4A) and (4B), where the asterisks designate the surface species.

$$AlOH* + Al(CH_3)_3 \rightarrow AlOAl(CH_3)_2* + CH_4 \quad (4A)$$

$$AlCH_3* + H_2O \rightarrow AlOH* + CH_4 \quad (4B)$$

The reactants trimethylaluminum (TMA, $Al(CH_3)_3$) and water are alternately injected via nitrogen carrier gas. Using computer-controlled pneumatic valves, the substrate surface is first exposed to TMA, which reacts with the active surface sites, Fig. 1 (a). Then, after purging the by-products from reaction (4A), the surface is

exposed to H_2O. This reaction regenerates the initial functional groups, preparing the surface for the next exposure to TMA, Fig. 1 (b). The film is grown to the desired thickness by repeating the AB sequence. For the 4.7 l chamber, the dose times of 1 and 0.2 s were utilized for TMA and H_2O, respectively, at the injection pressure of 300 mTorr. Dosing was followed by purging with ultrahigh purity N_2 at the injection pressure of 300 mTorr for 75 s. The dose and purge times of 1.5 and 120 s were used specifically for the leakage current structures (Fig. 4) to ensure surface exposure and prevent spurious reaction between chemical precursors, respectively. The growth temperature of 155 °C and baseline chamber pressure of 650 mTorr were used for all experiments. Direct deposition (with no substrate surface treatment) was performed after a 12 h stabilization at the deposition temperature.

Indentation of Al_2O_3 was performed at room temperature using a commercial instrument (Nano DCM, Agilent Technologies, Inc.) equipped with a diamond Berkovich tip. When measured in "continuous stiffness" mode (CSM, Ref. [52]), modulus and hardness can be evaluated at discrete instances (unloading events) throughout the measured depth range. Once the tip has engaged the material's surface, the instrument is capable of resolving load increments less than 1 μN, with displacement resolution less than 1 nm. The instrumented indentation method is accurate to within about 5–10% of the measured E and H values when multiple indentation measurements are averaged.

The details of the indentation experiments are as follows: indentation was performed to the depth of 100 nm for the 500 nm thick film on Si, to prevent cracking at the corners as well as to limit the influence of the substrate. The test procedure followed the trapezoidal profile [15] by: loading at the constant strain rate [53] of 0.05 (s^{-1}); holding at the maximum load for 30 s for stabilization; unloading at the constant strain rate of 0.05 (s^{-1}); and finally holding at 10% of the maximum load for 30 s to obtain a thermal drift correction. For all indentation experiments, test locations were offset by 100 μm to ensure isolation between the 30 separate sites.

Key details of the data reduction of the raw indentation measurements are as follows: immediately prior to the tests, the tip was calibrated against the elastic modulus of fused silica [14], with the area coefficients being chosen to achieve an optimum fit of the CSM data according to Eq. (5).

$$A[h_c] = \sum_{n=0}^{4} C_n (h_c)^{2-n} = C_0 h_c^2 + C_1 h_c + C_2 h_c^{1/2} + C_3 h_c^{1/4} + C_4 h_c^{1/8} \quad (5)$$

In Eq. (5), $A[h]$ represents the depth dependent area function (m^2) and C represents the area fit coefficient(s). The contact depth, h_c, was determined according to a linear fit of the measured P vs. h data, just after the tip was unloaded, Eq. (6).

$$h_c = h - \varepsilon \frac{P}{\boldsymbol{S}}\bigg|_{\text{unload}} \quad (6)$$

New parameters represented include h, which represents the measured depth (m); ε, the assumed sink-in parameter of 0.75 [14]; P, the applied load (N); and $\boldsymbol{S}$, the "harmonic contact stiffness" (i.e., $\partial P/\partial h$) (N/m). The effective modulus was evaluated at the instant the tip was unloaded according to Eq. (7) [14,15].

$$E_{\text{eff}} = \frac{\boldsymbol{S}\sqrt{\pi}}{2\beta\sqrt{A[h_c]}}\bigg|_{\text{unload}} \quad (7)$$

New parameters include, E_{eff}, which represents the effective modulus (Pa); and β, the tip geometry factor – assumed to be 1.05 based on Ref. [54]. For the two-dimensional axisymmetric analysis, the effective modulus was related to the elastic modulus of the specimen using Eq. (8).

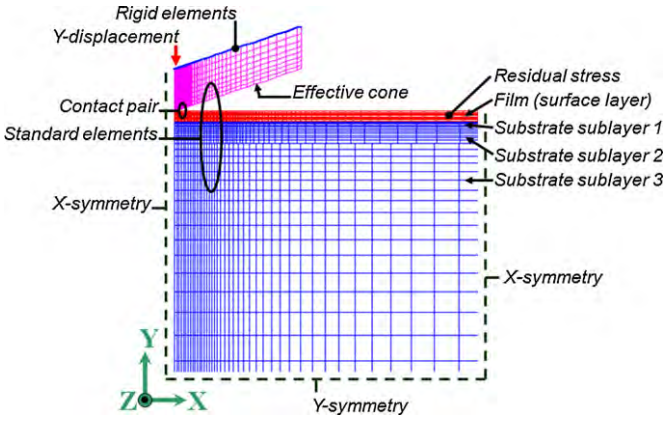

Fig. 2. Schematic summarizing key aspects of the FEA, including element types; the number of layers; initial conditions; and boundary conditions.

$$\frac{1}{E_{\text{eff}}} = \frac{1-\nu_f^2}{E_f} + \frac{1-\nu_i^2}{E_i} \quad (8)$$

In the equation, the subscripts f and i, refer to the film and the indenter tip, respectively. E_i and ν_i were assumed to be 1141 GPa and 0.07, respectively. ν_f was assumed to be 0.24 [26,55] (vs. $\nu_f = 0.13$ mistakenly identified in Ref. [8]). The Berkovich hardness, H, was evaluated at the instant the tip was unloaded according to Eq. (9).

$$H = \frac{P}{A[h_c]}\bigg|_{\text{unload}} \quad (9)$$

The raw load, depth, and harmonic contact stiffness data were utilized with a finite element analysis (FEA) protocol [56] that inherently incorporates the effect of the substrate and allows for interpretation at shallow depths, i.e., ≥20 nm. Because the fused silica calibration (i.e., Eq. (5)) does not ensure a positive area of contact at shallow depths, the tip was assigned an ideal spherical shape for $h \leq 1$ nm. For an assumed elastic/perfectly plastic constitutive behavior profile, the yield strength and modulus values are interpolated from a fit of the simulated stiffness and force relative to those measured at a particular depth, Eqs. (10) and (11).

$$\sigma_y = a_1 \boldsymbol{S} + b_1 P + c_1 \quad (10)$$

$$E = a_2 \boldsymbol{S} + b_2 P + c_2 \quad (11)$$

E and σ_y (therefore H) are determined iteratively from a set of initial guesses that bound the converged solution. To clarify, the parameter σ_y represents the yield strength of the film (Pa); $\boldsymbol{S}$, the harmonic contact stiffness (N/m); P, the applied load (N); and E, the modulus of the film (Pa). To facilitate rapid analysis, the measurements were binned and averaged at twenty depths throughout the range of the experiment, where the fitting coefficients a, b, and c are mathematically eliminated at each depth by the interpolation process. In the protocol, an equibiaxial stress (constant through the thickness of the film) can be assigned within the FEA in order to examine the influence of σ_f on E and σ_y [56]. The values of $E = 168$ GPa, $\nu = 0.22$, and $\sigma_y = 5270$ MPa were determined for the substrate (identical to Ref. [57]), from an analysis of an indented Si wafer. The value of $\nu = 0.24$ was assumed for the Al_2O_3 films.

Details of the FEA, including the geometry and boundary-conditions are summarized in Fig. 2. Computation was performed using a commercial code (ABAQUS, Dassault Systèmes Inc.) in conjunction with custom front-end utilities [56]. The simulated Berkovich tip (the 70.3° equivalent cone geometry for the two-dimensional axisymmetric condition [15]) was represented using

a set of 2-node rigid linear-link elements (RAX2) to apply a displacement to an adjoining set of standard 4-node bilinear elements (CAX4R). The film itself consisted of a single layer, 10 standard elements thick. While truncated in Fig. 2, the substrate was represented using three separate layers (thickness 1, 2, and $50h_f$) in order to refine accuracy in the region near the tip, while allowing the substrate to approach the semi-infinite condition on its far sides. The modeling of the substrate as a semi-infinite entity inherently accounts for its mechanical compliance. The element aspect ratio for the mesh (all layers) was varied in accordance from 0.5 near the tip to 5 at the far boundary in order to reduce the overall computation time. Nodes along the central- and far radial-axes (left and right of Fig. 2) were radially pinned and vertically free, whereas nodes along the bottom of the mesh (bottom of Fig. 2) were radially free and vertically pinned. An initial condition was used to specify the film stress. In the original work [56], when a film stress is not present the 4-node linear, non-reflecting one-way infinite element (CINAX4) was used (bottom and right of Fig. 2) to reduce the overall mesh size, while accurately representing the semi-infinite boundary condition. A contact analysis (assumed friction coefficient of 0.2) was assigned between the indenter and film. The FEA is run for an applied displacement ($h \pm 1$ nm to simulate the CSM method). The output parameters are the required net force on the tip and the resulting harmonic contact stiffness of the tip/specimen system. Other approaches for the analysis of the indentation of film/substrate systems exist, including solely analytic means [16,58–63] and numerical analysis [64–66]. The instrument measurements are normalized relative to the substrate properties for the FEA in Ref. [66].

A diamond cube-corner tip [15,18,19] was used to indent the 500 nm thick Al_2O_3 film on Si up to 400 nm, with a commercial instrument (Nanoindeter XP, Agilent Technologies, Inc.) and procedure similar to that described above (trapezoidal loading profile). The Nanoindeter XP is capable of resolving load increments less than 1 μN, with displacement resolution less than 1 nm. A 500 nm thick annealed plasma chemical vapor deposited (PCVD) tetraethylorthosilicate (TEOS) SiO_2 sample [67] was also indented for comparison. Here, the indentation parameter values of $\beta = 1.05$ and $\varepsilon = 0.75$ were also used. The tip calibration (conducted using fused silica) results in different area coefficients for the cube-corner tip, Eq. (5). Indentation was performed adjacent to a carbon paint mark so that the impression sites could be located quickly in a field emitting scanning electron microscope (FESEM). A sputtered Pt/Au coating ($h_f \sim 1$ nm) was added prior to indentation to aid FESEM imaging.

Al_2O_3 films, nominally 100 nm thick, were deposited on 300 μm thick, 100 mm diameter (1 0 0) Si wafers (University Wafer, Inc.) for curvature measurements (FLX 2320-S, Toho Technology Corp.). Si substrates were utilized because they are well characterized and are manufactured with high precision. The use of thin, large diameter wafers compensates the thickness and modulus of the Al_2O_3 film, Eq. (2). The FLX 2320-S measures radius of curvature based on the change in angle (incident vs. reflected) of a rastered laser. Linear scans ensure radius measurements to within 2.5% of the averaged value. The FLX 2320-S has a temperature controlled chuck, set here to record curvature at each 5 °C/min increment. To prepare the specimens for measurement, Al_2O_3 was removed from the backside of the wafer using highly basic (pH∼13) solutions of NaOH (from pellets), hydrogen peroxide (30 wt.%), and deionized water. The coating dissolved when repeatedly wiped with a solution soaked tissue, as verified visually from the indigo appearance of undissolved Al_2O_3. Before and after wafer curvature measurements, the film thickness and index of optical refraction were measured a small spot spectroscopic reflectometer (NanoSpec, Nanometrics, Inc.).

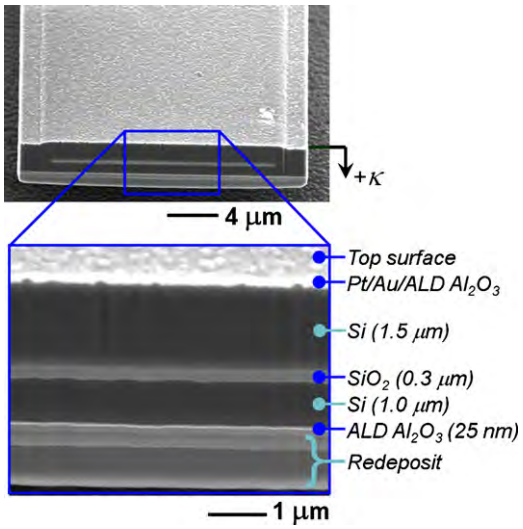

Fig. 3. Micrograph showing the cross-section of a microcantilever beam coated with Al_2O_3. The layers are labeled, including the material redeposited underneath by the FIB.

Similar to the wafer curvature characterization, Al_2O_3 was deposited on microcantilever beams in order to estimate film stress. The microcantilevers consisted of laminated polycrystalline silicon (polySi), SiO_2, and polySi layers nominally 1.5, 0.3, and 1.0 μm thick, respectively, Fig. 3. The figure shows an Al_2O_3 coated beam after it was cut across its width using a focused ion beam (FIB, Nova Nanolab, FEI Company). The layers present are labeled according to their contrast in the image, including the material redeposited during the ion milling process. The direction of positive curvature occurs for tip deflection towards the substrate, as indicated with an arrow in Fig. 3. Microcantilevers were fabricated on separate dice according to a standard microsystems technology (SUMMiT V, Sandia National Laboratories) [68]. Identical arrays of beams nominally 20 μm wide ranged in length from 100 to 550 μm in 50 μm increments. The microcantilevers were mechanically-freed from sacrificial SiO_2 layers by etching in a solution of 48 wt.% hydrofluoric acid (HF) and Triton-X 100 surfactant [69] for 20 min. As shown in Fig. 3, the middle SiO_2 layer of the beams is encased in Si, so that the SiO_2 is not removed in HF.

Because the beams are non-symmetric about their thickness, they exhibit an initial curvature of approximately −55 (m^{-1}). In contrast to the SUMMiT technology [68], the microcantilever method is not well suited for the MUMPs technology [70], because the nominal radius of curvature of polySi/SiO_2/polySi composite structures is roughly 43 (m^{-1}). That is, the tip of similar MUMPs beams will contact the substrate for lengths >200 μm. The curvature of the beams was measured using an interferometric microscope (New View 200, Zygo Corp.). The vertical resolution of the machine is better than 1 nm, while the lateral resolution for the 10× objective at 0.75× magnification is approximately 0.89 μm. The measurement accuracy of the instrument is therefore expected to be better than 1.2% (two standard deviations) for the beams studied. Curvature was measured immediately before and after deposition, so that the stress in the coating can be determined from the multilayer composite analysis [34–36].

The analysis procedure for the microcantilevers is formally described in Ref. [36]; the final step is to relate between microcantilever curvature and stress, Eq. (12). New parameters in the equation include *A*, the constant coupling axial extension between the layers (N); *D*, the bending coupling constant (N m^2); *B*, the constant coupling between extension and bending (N m); *N*, the term for the laminate force (N); and *M*, the term for the laminate bending

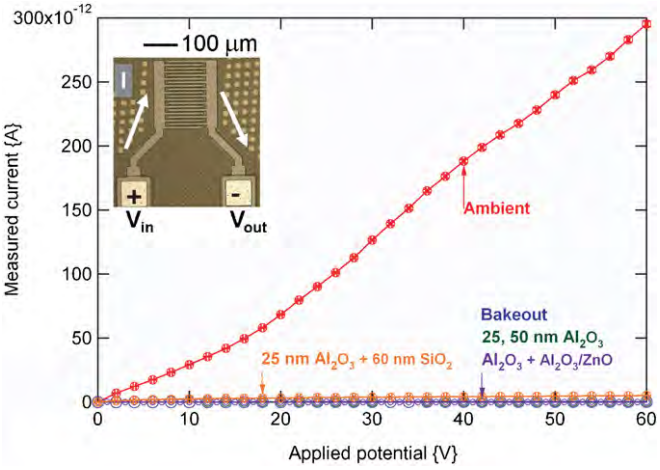

Fig. 4. Leakage current measurements for an interdigitated leakage current sensor. The inset contains an optical micrograph, showing the test structure from the top. The applied electrical conditions (I/V) indicated in the inset.

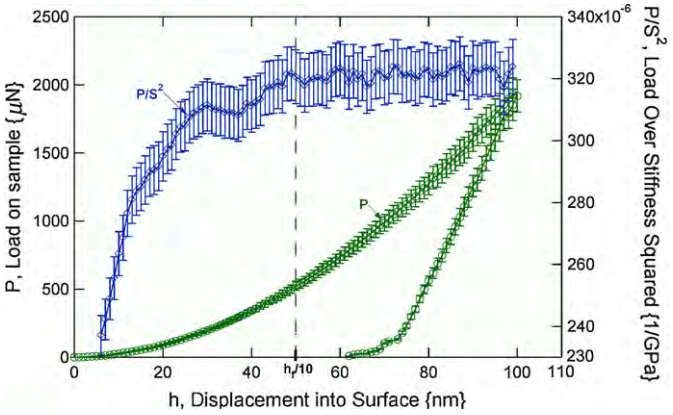

Fig. 5. Raw indentation results for 500 nm thick Al_2O_3 film on Si.

moment (N m). The coefficients A, B, and D vary with the E, ν, and h of each of the component layers. The terms N, and M vary with the E, ν, h, α, and σ of the component layers as well as ΔT. The analysis was simplified to the one-dimensional condition (layer width is eliminated) because the beam length was significantly greater than the width.

$$\Delta\kappa = \frac{(-BN) + (AM)}{(AD) - (B^2)} \tag{12}$$

3. Results

3.1. Leakage current assessment

ALD surface coatings are of interest as a moisture barrier enabling wafer level encapsulation (WLE) of microelectromechanical systems (MEMS). The WLE is formed by first globally depositing a sacrificial (SAC) layer and then locally patterning the SAC layer at the MEMS devices. Then an encapsulation structural layer, typically an oxide (LOX), is deposited over the sacrificial layer. The LOX is patterned and etched to expose the SAC layer that is subsequently removed by a sacrificial release process. In the next steps, the release etch holes are plugged and a sealing barrier layer is added. In the experiments here, supplemental ALD barrier films were added for evaluation in the absence of the final sealing barrier.

Evaluation of the WLE is performed using a leakage current monitor. The leakage current monitor is comprised of a series of interdigitated conductive fingers, as shown in Fig. 4 (inset). The interdigitated structure has traditionally enabled dew point detection during plastic package qualification [71–73]. After calibration in a temperature- and moisture-controlled environment, the same structure may function as a humidity sensor, whether encapsulated by a permeable polymeric layer [74] or direct exposed to the environment [75,76]. In the direct ambient, monolayers of water at the surface may facilitate electric current.

The leakage current monitor, Fig. 4, is fabricated at a commercial foundry from an Al layer with a line and space of 5 μm. The leakage current monitor is encapsulated at the wafer level so that ALD surface coatings can be added directly on the WLE to act as a barrier to moisture. This approach to validate the WLE has been previously used to examine thin film [74,77] and wafer bonded [75,76] encapsulation schemes.

As shown in Fig. 4, current/voltage traces were recorded in the ambient environment for uncoated sensors using a semiconductor parameter analyzer (Agilent Technologies, HP 4155B) with worst case accuracy of ±0.73%. In contrast to the uncoated ("ambient") condition, no signal was detected within the resolution of the instrument (1×10^{-14} A) for the same sensors immediately after they were baked at 200 °C for 24 h. No current was detected for sensors coated with 25 nm Al_2O_3, 50 nm Al_2O_3, or 25 nm Al_2O_3 + 25 nm Al_2O_3/ZnO. A slight leakage current, however, was detected for sensors coated with 25 nm Al_2O_3 + 60 nm SiO_2.

Fig. 4 demonstrates the utility of ALD coatings for encapsulation in applications where a hermetic package may not be physically possible or cost-effective. A monolayer of Al_2O_3 may provide moisture protection, preventing electrical shorting or spurious corrosion currents. The h_f of 25, and 50 nm were explored here for Al_2O_3 to ensure adequate breakdown voltage [78]. While Al_2O_3 is prone to corrode in strongly acidic or basic environments [79], Al_2O_3 may be used as the base layer for other inert materials – such as chemical vapor deposited SiO_2 [79]. Alternately, an electrically conductive Al_2O_3/ZnO composite may be deposited onto Al_2O_3 for the purpose of electric charge dissipation. For Al_2O_3/ZnO, the topmost layer is a ceramic composite [80] grown by alternating the deposition chemistry (8 cycles of Al_2O_3 and 5 cycles of ZnO), resulting in a 50% volumetric mixture. ZnO was grown here using the diethylzinc (DEZ, $Zn(CH_2CH_3)_2$) and H_2O chemistry system [80]. All of the aforementioned coatings proved very successful in reducing the leakage current relative to the uncoated configuration in the ambient condition. The distinct profile for the 25 nm Al_2O_3 + 60 nm SiO_2 coating may be caused by residual stress related cracking; the mechanism enabling leakage current was not specifically investigated.

3.2. Instrumented indentation

To understand the durability of the coatings in Fig. 4, the key thermo-mechanical properties were investigated. Binned and averaged indentation data is shown in Fig. 5, including the variation in P/S^2 and load with indentation depth. P/S^2 [81] is seen to asymptotically converge at about h = 50 nm. The initial P/S^2 profile (from h = 0–40 nm) identifies that the depth of contact is not sufficient to be readily represented using the standard analysis procedure, e.g., because of the imperfect geometry of the tip [14,82]. The more uniform behavior for h > 40 nm results from the mechanical characteristics of film followed by the film/substrate system. The slope of the P/S^2 profile at greater depths (e.g., h = 100 nm) may be used to assess the contribution of the substrate relative to that of the film. While the specimen was further indented up to $h_f/5$, the values of $E = 183.9 \pm 6.46$ and $H = 11.6 \pm 0.7$ GPa were determined for $h_f = 50 \pm 5$ nm. The P vs. h profile in Fig. 5 is typical of a ceramic material [14,15] and is comparable to that previously observed for ALD Al_2O_3 [83,84]. Because the raw E_f measurement slightly exceeds

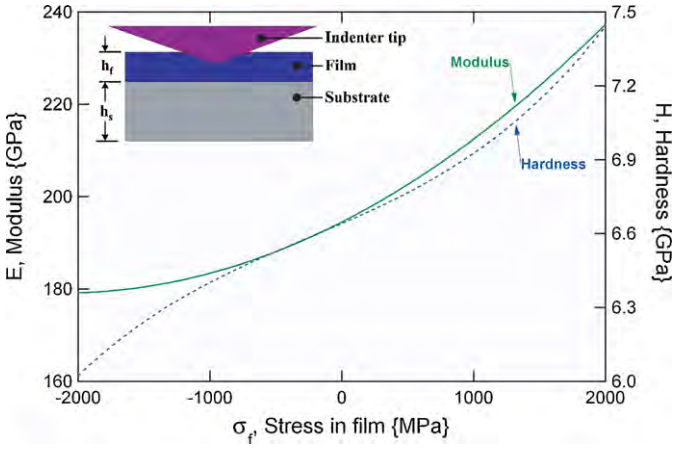

Fig. 6. Indentation results, analyzed for the 500 nm thick Al_2O_3 coating on Si.

E_s, and the film stress of 474 MPa has been previously measured for ALD Al_2O_3 [83], the indentation data was subjected to the numerical analysis protocol [56].

As shown in Fig. 6, the indentation data was evaluated over a broad range of σ_f conditions. To clarify, E and H in Fig. 6 were evaluated from the indentation data in Fig. 5 as a function of the σ_f that might be present. As described later, σ_f was independently verified to vary with temperature. In the figure, E is seen to vary monotonically. H further depends on inelastic material behavior and varies more complexly with stress in Fig. 6. Results for $\sigma_f = 0$ and $\sigma_f = 500$ MPa are given for reference in Table 1. The yield strength and corresponding strain, ε_y, are provided in the table for the assumed linear elastic limit.

To begin discussion of the indentation results, Fig. 6 and Table 1 identify minor variation with σ_f over the range of 500 MPa. For Al_2O_3, a 3.8 and 2.1% variation with σ_f is observed for E and H, respectively. Regarding variation in H with σ_f, the σ_f of 500 MPa comprises 10.2% of σ_y, Table 1, whereas the σ_f of 2000 MPa approaches 41% of σ_y. During applied tensile stress, the film becomes more inclined to flow during indentation, decreasing its hardness. The geometry of the residual impression is accurately rendered in FEA. The influence of geometry on E (occurring through $\boldsymbol{S}$ as well as the corresponding area of contact in Eq. (7)) is therefore considered in Fig. 6 and Table 1.

Regarding the E and H values in Table 1, they are similar to those previously measured for thin Al_2O_3 films. A survey of the literature in Ref. [83] identifies $100 < E < 272$ GPa and $8 < H < 9.6$ GPa for evaporated, chemical deposited, and vapor deposited Al_2O_3. A recent study specific to ALD Al_2O_3 identified the E and H values of 220 and 10.5 GPa, respectively, using an analytic model to account for the film/substrate geometry [84]. In comparison, the Hill modulus for untextured polycrystalline α-Al_2O_3 ("corundum") is 402.7 GPa [85], while the measured E for bulk amorphous Al_2O_3 is 372 GPa [86]. The modulus for ALD Al_2O_3 is decreased relative to the bulk value because of its amorphous nature [4]. That is, the density of ALD Al_2O_3 is 3.0 g/cm^3 [87], whereas that of bulk monocrystalline α-Al_2O_3 is 3.96 g/cm^3 [88]. While the complicated three-dimensional strain field invoked during indentation does not readily distinguish anisotropic property variation [89,90], the isotropic structure of ALD Al_2O_3 [4] prohibits such variation here.

Table 1
Summary of analysis results (average ± 2 SD) for 500 nm thick Al_2O_3 film on Si.

σ_f (MPa)	E_f (GPa)	H_f (GPa)	σ_y (MPa)	ε_y (%)
0	195.3 ± 20.1	6.65 ± 0.80	4,882 ± 679	2.5
500	202.7 ± 21.8	6.79 ± 0.79	5,177 ± 644	2.6

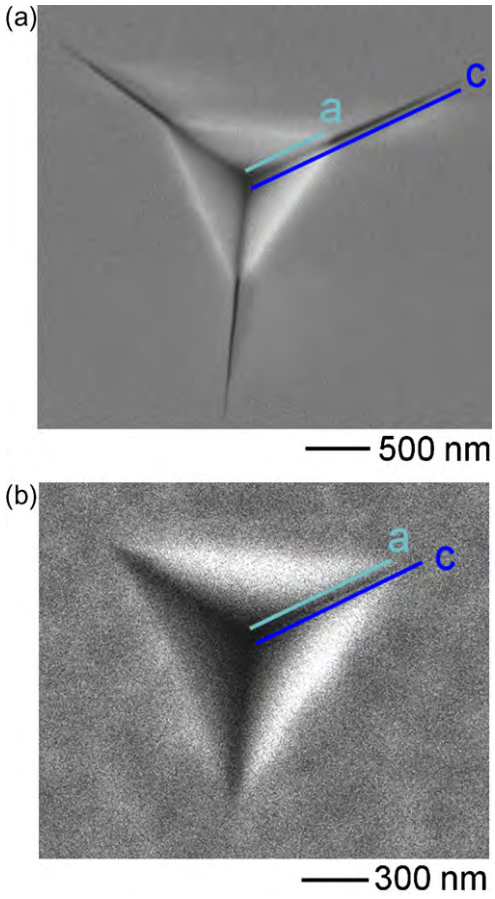

Fig. 7. FESEM images of the residual impression remaining after indentation to $h = 400$ nm using a cube-corner tip for 500 nm thick (a) Al_2O_3, and (b) SiO_2 coatings on Si.

The numerical analysis protocol also importantly identifies the influence of the substrate, which was not previously considered in Refs. [12,83]. The mechanical compliance of the substrate (occurring because $E_s < E_f$) increases E_f by 11.4 MPa (6.2%) over the raw measured value. In comparison, an additional increase of 7.4 MPa for the corrected E_f is identified for $\sigma_f = 0 \rightarrow 500$ MPa. Similar trends are observed for H_f, although the base value of 6.65 GPa (which accounts for substrate compliance) is less than that in previous studies [12,83,84]. While the $P/\boldsymbol{S}^2$ vs. h profile in Fig. 5 suggests that the film is largely decoupled from substrate, the minor effect of substrate compliance might have been anticipated from the slope of a least squares fit, applied in the vicinity of $h_f/10$. In comparison to the raw measured values, the FEA rendered valid (converged) data at 30 nm ($0.06 \times h_f$).

3.3. Indentation toughness

Representative examples of the residual impression remaining after cube-corner indentation are shown in Fig. 7 for the separate ALD Al_2O_3 and PCVD SiO_2 coatings. Radial cracking was observed at the corners of the Al_2O_3 impressions, beginning at indentation depth of 100 nm (for data sets of $h = 50$, 100, 200, 300, and 400 nm). Cracks for the SiO_2 impressions never became of sufficient length to be considered for analysis, i.e., $c/a > 2.5$ for $h \leq 0.4\,h_f$ or $(c - a) \geq 4h_f$ for $h \leq 0.4\,h_f$. Only the $h = 400$ nm data for Al_2O_3 became of sufficient length to be analyzed as a channel-cracked film. In no cases did the film/substrate systems spall, such that would invalidate the analysis. Analysis was conducted from the images of the impression site, as there was no indication of the onset of cracking in

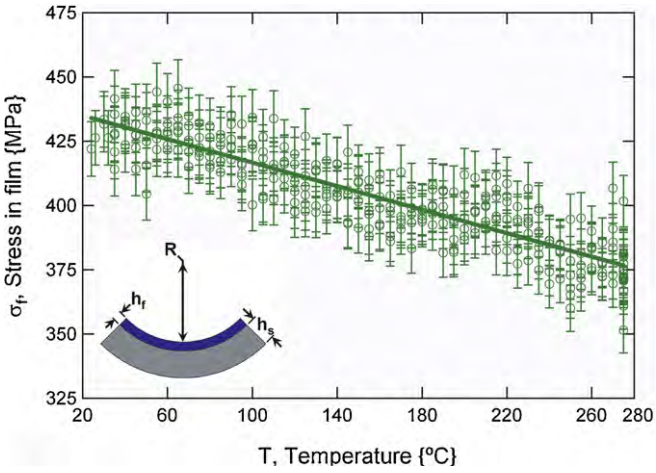

Fig. 8. Stress results over the first 3 consecutive thermal cycles for 100 nm Al_2O_3 deposited on Si. The specimen geometry for the wafer curvature measurements is shown in the inset.

the indentation data profiles according to the criteria of P vs. h [18]; load/stiffness squared ($P/\mathbf{S}^2$) vs. h [18,81]; K_{exp} vs. h [18,91]; or reduced stiffness (S^c) vs. h [18]. For $\lambda = 0.040$, $E_f = 195.3$ GPa, $\nu_f = 0.24$, $H_f = 6.65$ GPa, $h_f = 500$ nm, $E_s = 161.8$ GPa, and $\nu_s = 0.22$, the nominal K_{IC} of 0.76 ± 0.18 MPa $m^{0.5}$ was determined for $\sigma_f = 0$. If σ_f was allowed to vary, the K_{IC} of 1.89 MPa $m^{0.5}$ (measured previously in Ref. [8]) resulted for the tensile stress of 838 MPa.

A recent review discussing the limitations of estimating toughness via indentation [92] reminds that the legacy of the method owes to empirical means and not a theoretical origin. In particular, λ may vary according to the specimen material. Comparison against the SiO_2 specimen also suggests a significant tensile σ_f for the Al_2O_3 film, such that would aid corner cracking. (The SiO_2 specimen has the same geometry but different composition.) To explain, the SiO_2 [67] was annealed at high temperature, which would relax σ_f, making it less prone to cracking. Eq. (2) and (3) may be combined to estimate σ_f for the SiO_2 specimen, i.e., $\sigma_f = (E_f/(1-\nu_f))(\alpha_f - \alpha_s)\Delta T$. The values of $E_f = 70$ GPa, $\nu_f = 0.18$, $\alpha_f = 0.4$ ppm/°C, and $\alpha_s = 3.0$ ppm/°C imply $\sigma_f = -117$ MPa for SiO_2. Compressive σ_f (invoked after the SiO_2 cooled from the glassy state ($T_g \sim 550$ °C) to the ambient-temperature) would hinder crack formation. While the value of $\lambda = 0.040$ was utilized for the analysis above, the appropriate value is not well established in the literature for the cube-corner tip geometry. Eq. (1) renders $\lambda = 0.068 \pm 0.002$ for $K_{IC} = 1.89$ MPa $m^{0.5}$ if the tensile σ_f of 422–470 MPa is assumed for the Al_2O_3 film (see Fig. 8, below). Further study is warranted, because the technique in Fig. 7 is limited by the material dependent λ and process specific σ_f values.

3.4. Wafer curvature

Fig. 8 shows the stress present in Al_2O_3, measured using the wafer curvature method for three consecutive thermal cycles. The specimen was specifically heated to 275 °C and then actively cooled to 25 °C. The separate thermo-mechanical profiles cannot be readily distinguished in Fig. 8. The initial σ_f of 422 ± 21 MPa (present at the beginning of the first thermal cycle) was determined by comparing coated and uncoated wafers. During the all three thermal cycles, stress varied linearly with temperature. Similar response was observed in a separate specimen heated to 500 °C. The radius of curvature ranged from −150 to −340 m during the characterization in Fig. 8. Eq. (3) (applied to the least-squares fit in Fig. 8) identifies the CTE of 4.2 ± 0.1 ppm/°C for ALD Al_2O_3. A 2.5-nm thick native oxide [93] is expected to be present at the interface between Al_2O_3 and Si. This interlayer is expected to have negligible influence here, because it is symmetric (present on both the top- and bottom-Si surfaces) and is significantly thinner than h_f. The thickness of Al_2O_3 was determined by the reflectometer to be 101.9 and 102.3 nm before and after three thermal cycles, respectively. Similarly, the refractive indices of 1.641 and 1.640 were measured for Al_2O_3 before and after the experiment.

The CTE of 4.2 ppm/°C is less than that recently measured for amorphous Al_2O_3 thin films, where $\alpha = 7.1$ [26] and 5.0 ppm/°C [55]. For bulk Al_2O_3, the CTE of 5.1 and 6.6 ppm/°C has been identified for crystalline [94] and amorphous [86] material. The lesser α_f for ALD Al_2O_3 may owe to its density, which is roughly 3/4 that of fully dense crystalline material [87,88].

The estimates of CTE from Fig. 8 allow the contribution of thermal stress to be evaluated. The values of $E_f = 195.3$ GPa, $\nu_f = 0.24$, $\alpha_f = 4.2$ ppm/°C, and $\alpha_s = 3.0$ ppm/°C imply the tensile stress of 35 MPa is generated by cooling from the deposition temperature of 155 °C to the ambient. The contribution of thermal misfit is therefore estimated to be 5–10% of $\sigma_f = 422$ MPa. The remaining stress is attributed to other factors, such as film growth. For Al_2O_3, the parameter of temperature (but not pressure) affects the rate of growth according to the population of active surface sites [3]. Deposition temperature might therefore be used to manipulate σ_f. The added tensile stress of 67 MPa is predicted for the temperature change from 275 to 25 °C in Fig. 8.

The three overlapping κ vs. T profiles in Fig. 8 suggest ALD Al_2O_3 is stable over the temperature and time scale of the experiment. To clarify, material stabilization occurring during thermal cycling is common in thin films. Stabilization is motivated by mechanisms including grain growth, recrystallization, or (inter-/intra-) diffusion [37,95,96]. Material stabilization typically results in a complicated κ vs. T profile during the first thermal cycle. κ is then linear with T, so long as the previous T- or t-conditions are not exceeded. The h_f and n values before and after thermal cycling were identical (within the instrument accuracy), further suggesting that Al_2O_3 is stable. The curvature of microcantilever beams coated with Al_2O_3 (as in Fig. 3) was found in Ref. [97] to be unchanged over 4 months in the ambient environment, additionally suggesting that Al_2O_3 is stable with time.

3.5. Microcantilever curvature

Separate Al_2O_3 coatings of different thickness were grown on separate arrays of polySi/SiO_2/polySi microcantilever beams. For the microcantilevers of known thickness (Fig. 3), the parameters of $E_f = 195.3$ GPa, $\nu_f = 0.24$, $\alpha_f = 4.2$ ppm/°C, $E_{Si} = 161.8$ GPa, $\nu_{Si} = 0.22$, $\alpha_{Si} = 3.0$ ppm/°C, $E_{SiO_2} = 70.0$ GPa, $\nu_{SiO_2} = 0.18$, $\alpha_{SiO_2} = 0.4$ ppm/°C, and $\Delta T = 130$ °C were used in Eq. (12) to estimate σ_f. The residual stress in the two polySi layers in Fig. 3 was determined to be −2.8 and −4.3 MPa, respectively, using the pointer structure and procedure described in Ref. [98]. This may include the thermal contraction of polySi occurring between the deposition and ambient conditions. Residual stress in the SiO_2 layer was assumed to be 0. The σ_f values in Table 2 were determined from the difference in curvature before and after coating. The critical tensile stress required for channel-crack propagation, σ_c, is also shown in Table 2. σ_c was estimated for the Al_2O_3/Si system according to Beuth's model [27] using the parameters of $E_f = 195.3$ GPa, $\nu_f = 0.24$, $E_s = 161.8$ GPa, $\nu_s = 0.22$ and the mode I fracture toughness of 1.89 MPa $m^{0.5}$ for Al_2O_3 [8]. The σ_f estimates in Table 2 never exceed σ_c. Thermal misfit at the Al_2O_3/polySi interfaces is inherently incorporated into the results in Table 2, based on the temperature change between the deposition and ambient conditions. The contribution of thermal misfit became increasingly significant as h_f was decreased, affecting σ_f by 25% for

Table 2
Estimate of residual in-plane stress for Al_2O_3, from comparison of curvature before and after coating microcantilever beams. The implied through-thickness gradient may come from the geometry of the component layers as well as the morphology of the Al_2O_3/Si interfaces.

h_f, ALD Al_2O_3 (nm)	Measured ΔK (m^{-1})	σ_f (MPa)	σ_c (MPa)
10	2.18 ± 1.04	10140 ± 1120	13140
25	4.25 ± 1.11	4980 ± 500	8310
50	9.51 ± 2.60	3770 ± 600	5880
100	10.51 ± 1.36	2200 ± 180	4160
125	11.98 ± 1.56	2010 ± 180	370
500	4.07 ± 0.51	470 ± 50	1860

h_f = 10 nm. In Fig. 8 and Table 2, σ_f is importantly assumed to be constant through h_f.

The curvature values in Table 2 are troubling, not only because they imply the analysis of Fig. 8 is limited, but also because they are inconsistent with the measurements in Ref. [83]. The σ_f values in Table 2, however, should not be interpreted literally. The gradients implied in the table likely owe more to the mechanical structure of the microcantilevers than the characteristics of the component materials. To explain, the curvature of the microcantilevers occurs as the net deformation relieving the different stresses within each of the different thin films. A through-thickness strain gradient within the Al_2O_3 layer itself (incurred during the process of the formation of the Al_2O_3 layer) is not required to render the results in Table 2.

For the four films in Fig. 3, σ_f may occur because of stress remaining from the process of film formation; the morphology of the different film surfaces; lattice mismatch at the interfaces; and CTE-misfit at the interfaces. Significant σ_f may develop in chemical vapor deposited (CVD) films within the first 10–30 nm of material, owing to the process of island formation and coalescence [44–46]. Because the native oxide on Si will readily facilitate the initial generation of hydroxyl groups at the surface (Eq. (4A)), the island formation mechanism is not expected for the ALD Al_2O_3/polySi system.

The morphology of the different polySi film surfaces may greatly contribute to the deformation of the microcantilevers. Crevices are deeper (120 vs. 55 nm) and the surface roughness is greater (15.6 ± 12.8 nm vs. 5.4 ± 4.0 nm, for $R_{avg} \pm R_{rms}$) at the top and bottom surfaces of polySi, respectively [99]. The different porosity at the polySi surfaces dictates that a different volume of Al_2O_3 will exist adjacent to the top and bottom Al_2O_3/polySi interfaces. The different geometry present at the interfaces therefore allows a CTE motivated bending moment. In contrast, the surface of polished Si wafers lacks grain boundary grooves. Further, the roughness of Si wafers is typically on the order of 0.3 ± 0.4 nm [69], i.e., comparable to the ALD growth increment. While the argument of a mechanical bending moment enabled by the surface morphology in addition to the geometry and location of the component layers is not the only possible explanation, it does allow for significant σ_f in the absence of a through-thickness strain gradient for an ALD Al_2O_3/Si wafer system.

4. Conclusions

Interdigitated leakage current sensors with atomic layer deposited (ALD) coatings of (a) Al_2O_3, (b) Al_2O_3/SiO_2 layers, or (c) Al_2O_3/ZnO layers demonstrated no leakage current relative to uncoated sensors stored in the ambient. This identifies that ALD Al_2O_3 may be used to limit the effect of H_2O and other chemical species. To enable durability predictions, the thermo-mechanical properties of ALD Al_2O_3 were therefore investigated using indentation, wafer curvature, and microcantilever curvature measurements. Key results include:

For zero film stress, the elastic modulus of Al_2O_3 was determined to be 195.3 GPa using indentation, while the Berkovich hardness was 6.65 GPa. A 2–4% variation in modulus and/or hardness according to film stress was identified using a numerical analysis protocol. The variation with stress is about half of that associated with the mechanical compliance Si substrate, rendering the final corrected modulus and hardness of 202.7 and 6.79 GPa, respectively.

The coefficient of thermal expansion for Al_2O_3 was determined to be 4.2 ppm/°C using the wafer curvature method. The total stress present after deposition was 422 MPa. The tensile thermal stress invoked during cooling from the deposition temperature to the ambient was identified to be 35 MPa, i.e. 5–10% of the film stress. Stress decreased linearly during thermo-mechanical loading, but was not changed in the ambient condition despite repeated thermal cycling or temperature excursion to 500 °C. The thickness and index of refraction were unchanged after thermal cycling, suggesting Al_2O_3 is stable throughout the temperature range examined.

Separate $Si/SiO_2/Si$ microcantilever arrays demonstrated a curvature variation according to the thickness of Al_2O_3 coatings. The shape change is expected to depend on the geometry and location of the component layers as well as the different porosities at the top- and bottom-Si surfaces.

For the film stress of 422 MPa and mode I fracture toughness of 1.89 MPa $m^{0.5}$, the material-dependent geometry factor for cube-corner indentation may be as great as 0.068. In the absence of previously determined stress or toughness characteristics, the raw toughness of 0.74 MPa $m^{0.5}$ or tensile film stress of 838 MPa were independently identified here.

Acknowledgements

The authors are grateful to: Harkirat Guron of WiSpry, Inc for his help characterizing the interdigitated leakage current sensors, Dr. James Knapp of Sandia National Laboratories for his help with numerical analysis of indentation data, Dr. Dylan Morris of the National Institute of Standards and Technology for discussion concerning indentation toughness measurement, Mr. Fumio Kuruta and Dave Hurlbut of the Toho Technology Corporation for the use of the FLX2320 wafer curvature instrument, Dr. Byunghoon Yoon of the University of Colorado and Dr. Arrelaine Dameron of the National Renewable Energy Laboratory for feedback and discussion regarding the ALD and MLD techniques, Dr. Michael Dugger of Sandia National Laboratories for determination of the surface topology of the SUMMiT polycrystalline Si, as well as David Reyes of Block MEMS, LLC for the SUMMiT microcantilever specimens. This work was supported through the DARPA Center on NanoscaleScience and Technology for Integrated Micro/Nano-Electromechanical Transducers (iMINT) funded by DARPAN/MEMS S&T Fundamentals Program (HR0011-06-1-0048) (Dr. D.L. Polla, Program Manager). Study here is based upon work supported by the National Science Foundation under Grant No. IIP-0741177. Additional support was provided by the Air Force Office of Scientific Research.

Appendix A. Supplementary data

Supplementary data associated with this article can be found, in the online version, at doi:10.1016/j.sna.2010.09.018.

References

[1] M. Leskelä, M. Ritala, Atomic layer deposition (ALD): from precursors to thin film structures, Thin Solid Films 409 (2002) 138–146.
[2] M. Ritala, M. Leskela, Atomic layer deposition chemistry: recent developments and future challenges, Angew. Chem. Int. Ed. 42 (2003) 5538–5554.

[3] A.W. Ott, J.W. Klaus, J.M. Johnson, S.M. George, Al_2O_3 thin film growth on Si (1 0 0) using binary reaction sequence chemistry, Thin Solid Films 292 (1997) 135–144.
[4] J.W. Elam, M.D. Groner, S.M. George, Viscous flow reactor with quartz crystal microbalance for thin film growth by atomic layer deposition, Rev. Sci. Instrum. 73 (2002) 2981–2987.
[5] M. Hong, J. Kwo, Advanced high κ dielectrics for nano-electronics – science and technologies, ECS Trans. 1 (5) (2005) 41–60.
[6] M.D. Groner, S.M. George, R.S. McLean, P.F. Carcia, Gas diffusion barriers on polymers using Al_2O_3 atomic layer deposition, Appl. Phys. Lett. 88 (5) (2006) 051907.
[7] A.A. Dameron, S.D. Davidson, B.B. Burton, P.F. Carcia, M.R. Scott McLean, S.M. George, Gas diffusion barriers on polymers using multilayers fabricated by Al_2O_3 and rapid SiO_2 atomic layer deposition, J. Phys. Chem. C 112 (12) (2008) 4573–4580.
[8] D.C. Miller, R.R. Foster, Y.D. Zhang, S.H. Jen, J.A. Bertrand, Z.X. Lu, D. Seghete, J.L. O'Patchen, R.G. Yang, Y.C. Lee, S.M. George, M.L. Dunn, The mechanical robustness of atomic layer- and molecular layer-deposited coatings on polymer substrates, J. Appl. Phys. 105 (9) (2009) 093527.1–093527.12.
[9] C.F. Herrmann, F.H. Fabreguette, D.S. Finch, R. Geiss, S.M. George, Multilayer and functional coatings on carbon nanotubes using atomic layer deposition, Appl. Phys. Lett. 87 (12) (2005) 123110.
[10] H. Kim, H.B.R. Lee, W.-J. Maeng, Applications of atomic layer deposition to nanofabrication and emerging nanodevices, Thin Solid Films 517 (8) (2009) 2563–2580.
[11] J.W. Elam, D. Routkevitch, P.D. Mardilovich, S.M. George, Conformal coating on ultrahigh-aspect-ratio nanopores of anodic alumina by atomic layer deposition, Chem. Mater. 15 (18) (2003) 3507–3517.
[12] C.F. Herrmann, F.W. DelRio, D.C. Miller, S.M. George, V.M. Bright, J.L. Ebel, R.E. Strawser, R. Cortez, K.D. Leedy, Alternative dielectric films for RF MEMS capacitive switches deposited using atomic layer deposited Al_2O_3/ZnO alloys, Sens. Actuators A 135 (1) (2007) 262–272.
[13] N.D. Hoivik, J.W. Elam, R.J. Linderman, V.M. Bright, S.M. George, Y.C. Lee, Atomic layer deposited protective coatings for micro-electromechanical systems, Sens. Actuators A 103 (1–2) (2003) 100–108.
[14] W.C. Oliver, G.M. Pharr, Measurement of hardness and elastic modulus by instrumented indentation: advances in understanding and refinements to methodology, J. Mater. Res. 19 (2004) 3–20.
[15] A. Fischer-Cripps, Nanoindentation, Springer, New York, 2002.
[16] J. Menčík, D. Munz, E. Quandt, E.R. Weppelmann, Determination of elastic modulus of thin layers using nanoindentation, J. Mater. Res. 12 (9) (1997) 2475–2484.
[17] D.C. Miller, M.J. Talmage, K. Gall, Incipient yielding behavior during indentation for gold thin films before and after annealing, J. Mater. Res. 21 (10) (2006) 2480–2492.
[18] D.J. Morris, S.B. Myers, R.F. Cook, Sharp probes of varying acuity: instrumented indentation and fracture behavior, J. Mater. Res. 19 (1) (2004) 165–175.
[19] T. Chudoba, P. Schwaller, R. Rabe, J.-M. Breguet, J. Michler, Comparison of nanoindentation results obtained with Berkovich and cube-corner indenters, Philos. Mag. 86 (33–35) (2006) 5265–5283.
[20] B.R. Lawn, A.G. Evans, D.B. Marshall, Elastic/plastic indentation damage in ceramics: the median/radial crack system, J. Am. Ceram. Soc. 63 (9–10) (1980) 574–581.
[21] M.T. Laugier, Palmqvist crack extension and the center-loaded penny crack analogy, J. Am. Ceram. Soc. 68 (2) (1985) C51–C52.
[22] B.L. Lawn, Fracture of Brittle Solids, Cambridge University Press, New Cambridge, 1993, pp. 249–306.
[23] R.F. Cook, Strength and sharp contact fracture of silicon, J. Mater. Sci. 41 (2006) 841–872.
[24] R.D. Dukino, M.V. Swain, Comparative measurement of indentation fracture toughness with Berkovich and Vickers indenters, J. Am. Ceram. Soc. 75 (12) (1992) 3299–3304.
[25] J.M. Jungk, B.L. Boyce, T.E. Buchheit, T.A. Friedman, D. Yang, W.W. Gerberich, Indentation fracture toughness and acoustic energy release in tetrahedral amorphous carbon diamond-like thin films, Acta Mater. 54 (2006) 4043–4052.
[26] J. Thurn, R.F. Cook, Mechanical and thermal properties of physical vapour deposited alumina films, J. Mater. Res. 39 (2004) 4809–4819.
[27] J.L. Beuth, Cracking of thin bonded films in residual tension, Int. J. Solids Struct. 29 (13) (1992) 1657–1675.
[28] J.W. Hutchinson, Z. Suo, Mixed mode cracking in layered materials, in: J.W. Hutchinson, T.Y. Wu (Eds.), Advances in Applied Mechanics, vol. 29, Academic Press, San Diego, 1992, pp. 63–191.
[29] Z.C. Xia, J.W. Hutchinson, Crack patterns in thin films, J. Mech. Phys. Solids 48 (2000) 1107–1131.
[30] T. Nukamura, S. Kamath, Three-dimensional effects in thin film fracture, Mech. Mater. 13 (1992) 67–77.
[31] D.J. Morris, R.F. Cook, Indentation fracture of low-dielectric constant films. Part II. Indentation fracture mechanics model, J. Mater. Res. 23 (9) (2008) 2443–2457.
[32] G.G. Stoney, The tension of metallic films deposited by electrolysis, Proc. R. Soc. A82 (553) (1909) 172–175.
[33] M. Ohring, The Materials Science of Thin Films, Academic Press, San Diego, 1992, pp. 412–420.
[34] R. Jones, Mechanics of Composite Materials, second edition, Taylor & Francis, Philadelphia, 1999, pp. 224–229.
[35] T.W. Clyne, Encyclopedia of Materials: Science and Technology, vol. 9, Elsevier, New York, 2001, pp. 8126–8134.
[36] M.L. Dunn, S.J. Cunningham, Thermal and electromechanics of thin-film microstructures, in: Handbook of Nanotechnology, Springer-Verlag, New York, 2006.
[37] R.M. Keller, S.P. Baker, E. Arzt, Stress–temperature behavior of unpassivated thin copper films, Acta Mater. 47 (2) (1999) 415–426.
[38] J.A. Thornton, D.W. Hoffman, Internal stresses in titanium, nickel, molybdenum, and tantalum films deposited by cylindrical magnetron sputtering, J. Vac. Sci. Technol. 14 (1) (1977) 164–168.
[39] J.A. Thornton, D.W. Hoffman, Stress-related effects in thin films, Thin Solid Films 171 (1989) 5–31.
[40] P.J. Burnett, D.S. Rickerry, The scratch adhesion test: an elastic–plastic indentation analysis, Thin Solid Films 157 (2) (1988) 233–254.
[41] G.F. Cardinale, D.G. Howitt, K.F. McCarty, D.L. Medlin, P.B. Mirkarmi, N.R. Moody, Analysis of residual stress in cubic boron nitride thin films using micromachined cantilever beams, Diamond Relat. Mater. 5 (1996) 1295–1302.
[42] D.F. Bahr, J.W. Hoehn, N.R. Moody, W.W. Gerberich, Adhesion and acoustic emission analysis of failures in nitride films with a metal interlayer, Acta Mater. 45 (12) (1997) 5163–5175.
[43] N.R. Moody, D. Medlin, D. Boehme, D.P. Norwood, Film thickness effects on the fracture of tantalum nitride on aluminum nitride thin film systems, Eng. Fract. Mech. 61 (1998) 107–118.
[44] C.V. Thompson, R. Carel, Stress and grain growth in thin films, J. Mech. Phys. Solids 44 (5) (1996) 657–673.
[45] W.D. Nix, B.M. Clemens, Crystallite coalescence: a mechanism for intrinsic tensile stresses in thin films, J. Mater. Res. 14 (8) (1999) 3467–3473.
[46] F. Spaepen, Interfaces and stresses in thin films, Acta Mater. 48 (2000) 31–42.
[47] G.H. Gilmer, H. Huang, C. Roland, Thin film deposition: fundamentals and modeling, Comput. Mater. Sci. 12 (1998) 354–380.
[48] L.S. Shvindlerman, G. Gottstein, Cornerstones of grain structure evolution and stability: vacancies, boundaries, triple junctions, J. Mater. Sci. 40 (2005) 819–839.
[49] R.L. Puurunen, W. Vandervorst, W.F.A. Besling, O. Richard, H. Bender, T. Conard, C. Zhao, A. Delabie, M. Caymax, S.D. Gendt, M. Heyns, M.M. Viitanen, M. de Ridder, H.H. Brongersma, Y. Tamminga, T. Dao, T. de Win, M. Verheijen, M. Kaiser, M. Tuominen, Island growth in the atomic layer deposition of zirconium oxide and aluminum oxide on hydrogen terminated silicon: growth mode modeling and transmission electron microscopy, J. Appl. Phys. 96 (9) (2004) 4878–4889.
[50] O. Nilsen, O.B. Karlsen, A. Kjekshus, H. Fjellvåg, Simulation of growth dynamics in atomic layer deposition. Part I. Amorphous films, Thin Solid Films 515 (2007) 4527–4537.
[51] R.W. Wind, F.H. Fabreguette, Z.A. Sechrist, S.M. George, Nucleation period, surface roughness and oscillations in mass gain per cycle during W atomic layer deposition on Al_2O_3, J. Appl. Phys. 105 (2009) 074309.
[52] D.L. Joslin, W.C. Oliver, A new method for analyzing data from continuous depth-sensing microindentation tests, J. Mater. Res. 5 (1990) 123–126.
[53] B.N. Lucas, W.C. Oliver, Indentation power-law creep of high purity films, Metall. Trans. A 30 (1999) 601–610.
[54] J.H. Strader, S. Shim, H. Bei, W.C. Oliver, G.M. Pharr, An experimental evaluation of the constant ß relating the contact stiffness to the contact area in nanoindentation, Proc. Mater. Res. Soc. Symp. 841 (2005) R1.4.1–R1.4.6.
[55] J. Proost, F. Spaepen, Evolution of the growth stress, stiffness, and microstructure of alumina thin films during vapor deposition, J. Appl. Phys. 91 (1) (2002) 204–216.
[56] J.A. Knapp, D.M. Follstaedt, S.M. Meyers, J.C. Barbour, T.A. Friedmann, Finite-element modeling of nanoindentation, J. Appl. Phys. 85 (3) (1999) 1460–1474.
[57] D.M. Follstaedt, J.A. Knapp, S.M. Myers, Mechanical properties of ion-implanted amorphous silicon, J. Mater. Res. 19 (1) (2004) 338–346.
[58] R.B. King, Elastic analysis of some punch problems for a layered medium, Int. J. Solids Struct. 23 (12) (1987) 1657–1664.
[59] A.K. Bhattacharya, W.D. Nix, Analysis of elastic and plastic deformation associated with indentation testing of thin films on substrates, Int. J. Solids Struct. 24 (12) (1988) 1287–1298.
[60] H.Y. Yu, S.C. Sanday, B.B. Rath, The Effect of substrate on the elastic properties of films determined by the indentation test – axisymmetrical Boussinesq problem, J. Mech. Phys. Solids 38 (6) (1990) 745.
[61] D.S. Stone, Elastic rebound between an indenter and a layered specimen. I. Model, J. Mater. Res. 13 (11) (1998) 3207–3213.
[62] C. Shaohua, L. Lei, W. Tzuchiang, Nanoindentation of thin-film–substrate system: determination of film hardness and Young's modulus, Acta Mech. Sin. 20 (4) (2004) 383–392.
[63] P. Lemoine, J.P. Quinn, P.D. Maquire, J.F. Zhao, J.A. McLaughlin, Intrinsic mechancial properties of ultra-thin amorphous carbon layers, Appl. Surf. Sci. 253 (2007) 6165–6175.
[64] Z.-H. Xu, D. Rowcliffe, Finite element analysis of substrate effects on indentation behavior of thin films, Thin Solid Films 447–448 (2004) 399–405.
[65] J.S. Wang, X.J. Zheng, H. Zheng, Z. Zhu, S.T. Song, Evaluation of the substrate effect on indentation behavior of film/substrate system, Appl. Surf. Sci. 256 (2010) 5998–6002.
[66] J. Hay, Measuring Substrate-Independent Properties of Dielectric Films, Agilent Technologies, 2006.
[67] F.W. DelRio, M.L. Dunn, M.P. de Boer, Growth of silicon carbide nanoparticles using tetraethylorthosilicate for microelectromechanical systems, Electrochem. Solid-State Lett. 10 (1) (2007) H27–H30.

[68] J.J. Sniegowski, M.P. DeBoer, IC-compatible polysilicon surface micromachining, Annu. Rev. Mater. Sci. 30 (2000) 299–333.
[69] D.C. Miller, B.L. Boyce, P.G. Kotula, C.R. Stoldt, Connections between morphological and mechanical evolution during galvanic corrosion of micromachined polycrystalline and monocrystalline silicon, J. Appl. Phys. 103 (2008) 123518.
[70] J. Carter, A. Cowen, B. Hardy, R. Mahadevan, M. Stonefield, S. Wilcenski, PolyMUMPs Design Handbook: Revision 11, MEMSCAP Inc., 2005.
[71] M.G. Kovac, D. Chleck, P. Goodman, A new moisture sensor for in-situ monitoring of sealed packages, Solid-State Technol. 21 (2) (1978) 35–39.
[72] R. Fenner, E. Zdankiewicz, Micromachined water vapor sensors: a review of sensing technologies, IEEE Sens. J. 1 (4) (2001) 309–317.
[73] L.T. Nguyen, A.S. Chen, D. Quearry, D.W. Peterson, J.F. Reilly, Moisture sensing and stress test chips for plastic packaging qualification, in: Proceedings of Surface Mount International Conference, 1996, pp. 593–606.
[74] D.I. Forehand, C.L. Goldsmith, Wafer level micro-encapsulation, in: Proceedings of Govt. Microcircuit Applications and Critical Technology Conference, 2005, pp. 320–323.
[75] B. Ziaie, J.A. Von Arx, M.R. Dokmeci, K. Najafi, A hermetic glass–silicon micropackage with high-density on-chip feedthroughs for sensors and actuators, J. Microelectromech. Syst. 5 (3) (1996) 166–179.
[76] A. Margomenos, L.P.B. Katehi, Fabrication and accelerated hermeticity testing of an on-wafer package for RF MEMS, IEEE Trans Microwave Theory and Technology 52 (6) (2004) 1626–1636.
[77] D.I. Forehand, C.L. Goldsmith, Wafer level micropackaging for RF MEMS switches, in: Proc. IPACK, 2005, pp. 1–5.
[78] M.D. Groner, J.W. Elam, F.H. Fabreguette, S.M. George, Electrical characterization of thin Al_2O_3 films grown by atomic layer deposition on silicon and various metal substrates, Thin Solid Films 413 (2002) 186–197.
[79] A.A. Dameron, D. Seghete, B.B. Burton, S.D. Davidson, A.S. Cavanagh, J.A. Bertrand, S.M. George, Molecular layer deposition of alucone polymer films using trimethyaluminum and ethylene glycol, Chem. Mater. 20 (10) (2008) 3315–3326.
[80] J.W. Elam, Z.A. Sechrist, S.M. George, ZnO/Al_2O_3 nanolaminates fabricated by atomic layer deposition: growth and surface roughness measurements, Thin Solid Films 414 (2002) 43–55.
[81] T.F. Page, G.M. Pharr, J.C. Hay, W.C. Oliver, B.N. Lucas, E. Herbert, L. Riester, Nanoindentation characterization of coated systems. $P{:}S^2$ – a new approach using the continuous stiffness technique, Proc. MRS 522 (1998) 53–64.
[82] R. Saha, W.D. Nix, Effects of the substrate on the determination of thin film mechanical properties by nanoindentation, Acta Mater. 50 (2002) 23–38.
[83] M.K. Tripp, C. Stampfera, D.C. Miller, T. Helbling, C.F. Herrmann, C. Hierold, K. Gall, S.M. George, V.M. Bright, The Mechanical properties of atomic layer deposited alumina for use in micro- and nano-electromechanical systems, Sens. Actuators A 130–131 (2006) 419–429.
[84] K. Tapily, J.E. Jakes, D.S. Stone, P. Shresta, D. Gue, H. Baumgart, A.A. Elmustafa, Nanoindentation investigation of H_fO_2 and Al_2O_3 films grown by atomic layer deposition, J. Mater. Res. 155 (7) (2008) H545–H551.
[85] J.P. Watt, L. Pesselnick, Clarification of the Hashin Shtrikman bounds on the effective elastic moduli of polycrystals with hexagonal, trigonal, and tetragonal symmetries, J. Appl. Phys. 51 (3) (1980) 1525–1531.
[86] J. King, Materials Handbook for Hybrid Microelectronics, Artech House, Boston, 1988.
[87] M.D. Groner, F.H. Fabreguette, J.W. Elam, S.M. George, Low temperature Al_2O_3 atomic layer deposition, Chem. Mater. 16 (2004) 639–645.
[88] American Institute of Physics Handbook, American Institute of Physics, New York, 1982.
[89] J.J. Vlassak, W.D. Nix, Measuring the elastic properties of anisotropic materials by means of indentation experiments, J. Mech. Phys. Solids 42 (8) (1994) 1223–1245.
[90] J.J. Vlassak, M. Ciavarella, J.R. Barber, X. Wang, The Indentation modulus of elastically anisotropic materials for indenters of arbitrary shape, J. Mech. Phys. Solids 51 (2002) 1701–1721.
[91] M.R. McGurk, T.F. Page, Using the P-d^2 analysis to deconvolute the nanoindentation response of hard-coated systems, J. Mater. Res. 14 (1999) 2283–2295.
[92] G.C. Quinn, R.C. Bradt, On the Vickers indentation fracture toughness test, J. Am. Ceram. Soc. 90 (3) (2007) 673–680.
[93] M.J. Madou, Fundamentals of Microfabrication. The Science of Miniaturization, second edition, CRC Press, New York, 2002.
[94] Y.S. Touloukian, Thermal expansion – non-metallic solids, in: Thermophysical Properties of Matter, Plenum, New York, 1979.
[95] D. Gardner, P. Flinn, Mechanical stress as a function of temperature in aluminum films, Proc. IEEE Trans. Electron Devices 35 (12) (1988) 2160–2169.
[96] D.C. Miller, C.F. Herrmann, H.J. Maier, S.M. George, C.R. Stoldt, K. Gall, Thermomechanical evolution of multilayer thin films. Part 1. Mechanical behavior of Au/Cr/Si microcantilevers, Thin Solid Films 515 (2007) 3208–3223.
[97] D.C. Miller, R.R. Foster, S.H. Jen, J.A. Bertrand, D. Seghete, B.H. Yoon, Y.C. Lee, S.M. George, M.L. Dunn, Thermo-mechanical properties of aluminum alkoxide (alucone) films, created using molecular layer deposition, Acta Mater. 57 (2009) 5083–5092.
[98] D.C. Miller, B.L. Boyce, M.T. Dugger, T.E. Buchheit, K. Gall, Properties of a commercially available silicon-on-insulator MEMS material, Sens. Actuators A 138 (1) (2007) 130–144.
[99] M.T. Dugger, Private communication, March 6 (2009).